Nano-Micro Letters

ISSN 2311-6706
e-ISSN 2150-5551
CN 31-2103/TB

ARTICLE

https://doi.org/10.1007/s40820-019-0261-5

Cite as
Nano-Micro Lett.
(2019) 11:31

Received: 26 January 2019
Accepted: 15 March 2019

Ultrathin $Ti_3C_2T_x$ (MXene) Nanosheet-Wrapped $NiSe_2$ Octahedral Crystal for Enhanced Supercapacitor Performance and Synergetic Electrocatalytic Water Splitting

Hanmei Jiang[1,2], Zegao Wang[1,3], Qian Yang[4], Luxi Tan[2], Lichun Dong[2] ✉,
Mingdong Dong[1] ✉

Hanmei Jiang and Zegao Wang have contributed equally to this work.

✉ Lichun Dong, lcdong72@cqu.edu.cn; Mingdong Dong, dong@inano.au.dk

[1] Interdisciplinary Nanoscience Center (iNANO), Aarhus University, 8000 Aarhus-C, Denmark

[2] School of Chemistry and Chemical Engineering, Key Laboratory of Low-grade Energy Utilization Technologies and Systems of the Ministry of Education, Chongqing University, Chongqing 400044, People's Republic of China

[3] College of Materials Science and Engineering, Sichuan University, Chengdu 610065, People's Republic of China

[4] College of Chemistry and Molecular Engineering, Peking University, Beijing 100871, People's Republic of China

HIGHLIGHTS

- A strong interfacial chemical interaction between the $NiSe_2$ nanocrystal and $Ti_3C_2T_x$ MXene nanosheet ($NiSe_2/Ti_3C_2T_x$) was established by wrapping $NiSe_2$ octahedral crystal with ultrathin $Ti_3C_2T_x$ MXene nanosheet.
- $NiSe_2/Ti_3C_2T_x$ hybrid exhibits excellent performance and cycling stability both in supercapacitor and hydrogen evolution reaction.
- $NiSe_2$ nanocrystals are stabilized by the covering of $Ti_3C_2T_x$ MXene nanosheet which served as a protective layer from its oxidation.

ABSTRACT Metal selenides, such as $NiSe_2$, have exhibited great potentials as multifunctional materials for energy storage and conversation. However, the utilization of pure $NiSe_2$ as electrode materials is limited by its poor cycling stability, low electrical conductivity, and insufficient electrochemically active sites. To remedy these defects, herein, a novel $NiSe_2/Ti_3C_2T_x$ hybrid with strong interfacial interaction and electrical properties is fabricated, by wrapping $NiSe_2$ octahedral crystal with ultrathin $Ti_3C_2T_x$ MXene nanosheet. The $NiSe_2/Ti_3C_2T_x$ hybrid exhibits excellent electrochemical performance, with a high specific capacitance of 531.2 F g^{-1} at 1 A g^{-1} for supercapacitor, low overpotential of 200 mV at 10 mA g^{-1}, and small Tafel slope of 37.7 mV dec^{-1} for hydrogen evolution reaction (HER). Furthermore, greater cycling stabilities for $NiSe_2/Ti_3C_2T_x$ hybrid in both supercapacitor and HER have also been achieved. These significant improvements compared with unmodified $NiSe_2$ should be owing to the

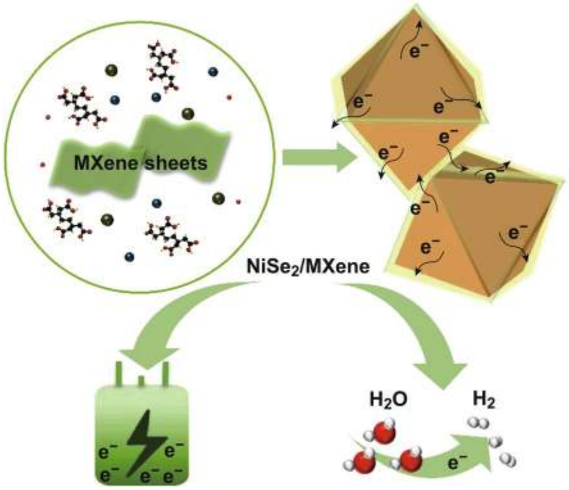

strong interfacial interaction between $NiSe_2$ octahedral crystal and $Ti_3C_2T_x$ MXene, which provides enhanced conductivity, fast charge transfer as well as abundant active sites, and highlight the promising potentials in combinations of MXene with metal selenides for multifunctional applications such as energy storage and conversion.

KEYWORDS MXene; $NiSe_2$; Supercapacitor; Water splitting

1 Introduction

With the development of society, the energy crisis has become more and more prominent; thus, developing strategies toward high efficient energy storage and energy conversion has caught much attention [1, 2]. Owing to its high power density, long cycling life, and rapid charge–discharge rates, supercapacitors (SCs) have stand out as one of the most promising candidates for energy storage [3]. Hydrogen, as a clean and renewable energy, is considered as a promising candidate to overcome the environmental issues. Recently, the hydrogen generation through hydrogen evolution reaction (HER) is considered as one most cost-optimal energy conversion technique [4]. Nevertheless, to date, the state-of-the-art materials for electrochemical processes in energy storage or conversion, such as the SCs or HER, are still mostly based on noble metal-based materials [5, 6]. The rare storage and high cost of these materials severely restrict their practical applications. Therefore, non-noble metal-based materials with high capacitance and low activation energy for energy storage and renewable energy are profoundly needed to replace noble metal materials [7–9]. Moreover, developing a material with both energy storage and conversion could not only save the cost but also facilitate its integration. Recently, it has been reported that transitional metal oxides [10], hydroxides [11] and their hybrids [12, 13] have been widely investigated demonstrating their potential application in both energy storage and conversion. However, the low electronic conductivity and poor cycling stability still limit their application [14].

By contrast, transition metal selenides, with their high electrochemical activity as well as excellent thermal stability, might be a possible substitute for noble metal materials [15–18]. In particular, nickel selenides ($NiSe_2$) not only have exhibited considerable potential in lithium-ion batteries [19–21], SCs [22–25], electrocatalyst [26–28] and photovoltaic [29], but also provided efficient HER function as the electrode materials [30]. Previous research suggested that the good electrochemical activity of nickel selenides should be owing to the unique electronic structure and multiple oxidation states. However, pure $NiSe_2$ exhibits unsatisfying cycling stability, low electrical conductivity, and insufficient electrochemically active sites [31]. Therefore, hybriding with new materials is considered as the promising method to overcome the drawback.

Carbonaceous materials such as carbon nanowires [32] and reduced graphene oxide (rGO) [33, 34] are considered favorable hybridizers for enhancing the conductivity, yet their intrinsic nature usually limits the capacities for energy storage [35, 36]. Therefore, developing new conductivity materials beyond carbonaceous materials for future energy storage and producing renewable energy poses a major challenge. As recently reported, MXene, a new family of two-dimensional (2D) transitions, metal carbides, carbonitrides with the general formula of $M_{n+1}X_nT_x$ (M is an early transition metal, X is C/N, and T_x is surface terminal groups such as hydroxyl (–OH) and fluorine (–F), etc.) have been introduced [37, 38]. In possession of the metallic conductivity with hydrophilic nature, which is seldom realized by many other 2D materials such as layered metal sulfides and graphene [39–41], MXenes have exhibit promising potential in lithium batteries and supercapacitors when hybridized as supporting materials [42–45]. For producing renewable energy, MXene with C_3N_4, Co-BDC MOF or MoS_2 also displays superb electrocatalytic activity [46–48]. Nevertheless, MXene hybrid systems are rarely investigated. To our best of knowledge, their combinations with metal selenides have not yet been reported. In this work, a novel electrode material based on $NiSe_2$ octahedral crystal wrapped with ultrathin $Ti_3C_2T_x$ MXene nanosheet was prepared via a simple one-pot hydrothermal route, where the hybridized $NiSe_2/Ti_3C_2T_x$ exhibits unique multifunction property in energy storage and conversion. The results show that the hybridized $NiSe_2/Ti_3C_2T_x$ displays excellent performances with capacity of 531.2 F g^{-1} at 1 A g^{-1} for supercapacitors, which is among the highest performances of the modified metal selenides [49, 50], and it also exhibits relatively smaller Tafel slope of 37.7 mV dec^{-1} for HER, which is close to the value of Pt.

https://doi.org/10.1007/s40820-019-0261-5

Further investigations have reviewed that these high performances of $NiSe_2/Ti_3C_2T_x$ are owing to the unique structure of the hybrid in which the $Ti_3C_2T_x$ MXene is evenly wrapped on the surface of the $NiSe_2$ octahedral crystal via an interfacial interaction. Compared with pure $NiSe_2$, such connection between the two compositions not only provides much faster charge transfer, but also increases durability as well.

2 Experimental Section

2.1 Reagent and Materials

Ti_3AlC_2 (98%) was purchased from the Forsman Scientific Co., Ltd. (Beijing, China). Polyvinylidene fluoride (≥ 99.5%) was purchased from Micxy Chemical Co., Ltd. (Chengdu, China). Nickel form (110 mesh per inch) was purchased from Chuan Dong Chemical Co., Ltd. (Chongqing, China). Carbon black was purchased from Cabot Corporation (Boston, USA). Hydrochloric acid (HCl, ACS grade, 36-38%), lithium fluoride (LiF, ACS grade, ≥ 99%), *n*-methyl-2-pyrrolidone (ACS grade, ≥ 99.8%), $NiCl_2$ (ACS grade, ≥ 99%), Se powder (ACS grade, ≥ 99%), KOH (ACS grade, ≥ 99%), and EDTA-Na_2 (ACS grade, ≥ 99%) were purchased from Sigma-Aldrich. All chemical materials were used as received without further purification.

2.2 Synthesis of $Ti_3C_2T_x$ Nanosheets

$Ti_3C_2T_x$ nanosheets were prepared according to previous literature, by the selective etching of the Al layer of Ti_3AlC_2 using a mixture of concentrated HCl and LiF [41]. Briefly, 2 g of LiF was slowly added and dissolved into 20 mL of 9 mol L^{-1} HCl under stirring to prepare the etching solution. Then, 2 g of Ti_3AlC_2 powders was carefully added to the solution over the course of 10 min to avoid overheating. The reaction mixture was heated to 40 °C for 48 h, and then the resulting solid was thoroughly washed using deionized (DI) water for more than three times until the pH value of the supernatant liquid reached 6–7 after the centrifugation. The final $Ti_3C_2T_x$ powder was obtained after drying the raw materials at 60 °C under vacuum for 12 h. And then, 100 mg of $Ti_3C_2T_x$ powder was added to 10 mL of water. After sonication 1 h under Ar bubbling, the $Ti_3C_2T_x$ sheet solution (10 mg mL^{-1}) was formed and stored in fridge for further using.

2.3 Synthesis $NiSe_2/Ti_3C_2T_x$ Hybrid

The $NiSe_2/Ti_3C_2T_x$ hybrid was synthesized by a one-pot hydrothermal method [27, 51]. Briefly, 2 mmol Se powder was firstly dissolved by 5 mL KOH solution (20 mol L^{-1}) to form a brownish red solution. Subsequently, 1 mmol $NiCl_2$ was dissolved in 19 mL DI water and mixed with 1.6 mmol EDTA-2Na (as chelating agent) to form a blue solution. Then 1 mL $Ti_3C_2T_x$ sheets solution (10 mg mL^{-1}) was added into the blue solution and ultrasonically dispersed for 30 min and then dropwisely added into the above brownish red solution. The as-prepared solution was transferred into a 50-mL Teflon-lined autoclave and heated at 180 °C for 24 h. After the reaction finished, the precipitates were collected by centrifugation and washed with DI water for several times until the pH value of the supernatant liquid reaches 7. Finally, the $NiSe_2/Ti_3C_2T_x$ hybrid was obtained by vacuum drying at 60 °C for 12 h. For comparison, unmodified $NiSe_2$ was synthesized by following the same method but without adding $Ti_3C_2T_x$ nanosheets.

2.4 Characterization

X-ray diffraction (XRD) analyses were performed on a Rigaku D/MAX-r diffractometer with Cu Kα radiation ($\lambda = 0.1541$ nm). Raman spectra were measured using a Renishaw via Raman microscope with the excitation laser line at 514 nm. X-ray photoelectron spectra (XPS) were recorded on a Kratos Axis Ultra DLD spectrometer equipped with a monochromatic Al Kα X-ray source (75–150 W), and C 1*s* (284.8 eV) was used to calibrate all the XPS peaks before comparison. Scanning electron microscopy (SEM, NOVA-667) and transmission electron microscopy (TEM, Talos FEI) were used to study the morphology of the samples. High-angle annular dark-field scanning transmission electron microscopy (HAADF-STEM, Talos) was used to identify the elemental composition of the samples.

2.5 Electrochemical Measurements

Both supercapacitor and HER performance of the as-synthesized $NiSe_2/Ti_3C_2T_x$ hybrid were evaluated at room temperature in the three-electrode system on a CHI660E workstation. For supercapacitor measurement, to prepare the working electrode, $NiSe_2/Ti_3C_2T_x$ or $NiSe_2$ powders (80 wt%), carbon black (10 wt%), and polyvinylidene fluoride (10 wt%) were dispersed in *n*-methyl-2-pyrrolidone, and then the resulted slurry was coated onto a piece of nickel form (1.0 × 1.0 cm^2), which was dried at 120 °C under vacuum for 12 h and pressed under 10 MP for 1 min to obtain the working electrode. The mass loading of $NiSe_2/Ti_3C_2T_x$ on the nickel foam was about 8 mg. The Ag/AgCl electrode and platinum wire were used as the reference and counter electrodes, respectively. The electrochemical measurements were performed in 2 M KOH aqueous solution. The cyclic voltammetry (CV) was carried out in the potential range of − 0.2 to 0.55 V versus Ag/AgCl electrode at a scan rate from 10 to 100 mV s^{-1}. The galvanostatic charge–discharge (GCD) was also performed in the potential range of − 0.2 to 0.55 V versus Ag/AgCl electrode. The electrochemical impedance spectroscopy (EIS) was performed in the range of 10 mHz to 100 kHz with potential amplitude of 10 mV. The specific capacitance in the three-electrode system was calculated from the GCD according to Eq. 1 [52].

$$C_s = \frac{I\Delta t}{m\Delta V} \tag{1}$$

where C_s (F g^{-1}) is the specific capacitance, I (A) is the discharge current, Δt (s) is the discharge time, m (g) is the total active material mass on the electrode, and ΔV (V) is potential window during the discharge process.

For electrocatalytic reaction, 6 mg of active material ($NiSe_2/Ti_3C_2T_x$ hybrid, $NiSe_2$, $Ti_3C_2T_x$) and 15 μL of Nafion solution were added into 160 μL mixed solvent of deionized water and isopropanol with a volume ratio of 5:3. The dispersive process lasted for 1 h by sonication to form a homogeneous ink. Then, 1.5 μL of the ink was loaded onto a 3-mm-diameter glassy carbon electrode. The whole electrochemical measurement process was in 0.5 M H_2SO_4 electrolyte, using a graphite as counter electrode, an Ag/AgCl electrode as reference electrode, and the above glassy carbon containing catalyst film as the working electrode. All measured potentials versus Ag/AgCl were transferred to reversible hydrogen electrode (RHE) based on the Nernst equation: $E(\mathrm{RHE}) = E(\mathrm{Ag/AgCl}) + 0.0592\,\mathrm{pH} + 0.197$. The linear scan voltammogram (LSV) curves were obtained by sweeping potential from 0 to − 0.7 V versus Ag/AgCl with a scan rate of 5 mV s^{-1}. EIS was carried out under the similar parameter settings as supercapacitor. The electrical double-layer capacitance (C_{dl}) of as-prepared electrodes was obtained using cyclic voltammograms (CVs) in a non-faradaic potential range (0.4 to 0.5 V vs. RHE). The stability test was measured by the continuous CV with scan rate of 100 mV s^{-1} for 2000 times. After cycling, the polarization curve was measured again. The chronoamperometry current density–time curve was measured in a constant potential of − 0.25 V versus RHE.

3 Result and Discussion

3.1 Synthesis and Characterizations of $NiSe_2$ and $Ti_3C_2T_x/NiSe_2$

The brief synthetic procedure of $Ti_3C_2T_x$ caped $NiSe_2$ hybrid is shown in Scheme 1. The $Ti_3C_2T_x$ MXene nanosheets (Figs. S1 and S2) were mixed within $NiCl_2$/EDTA and Se/

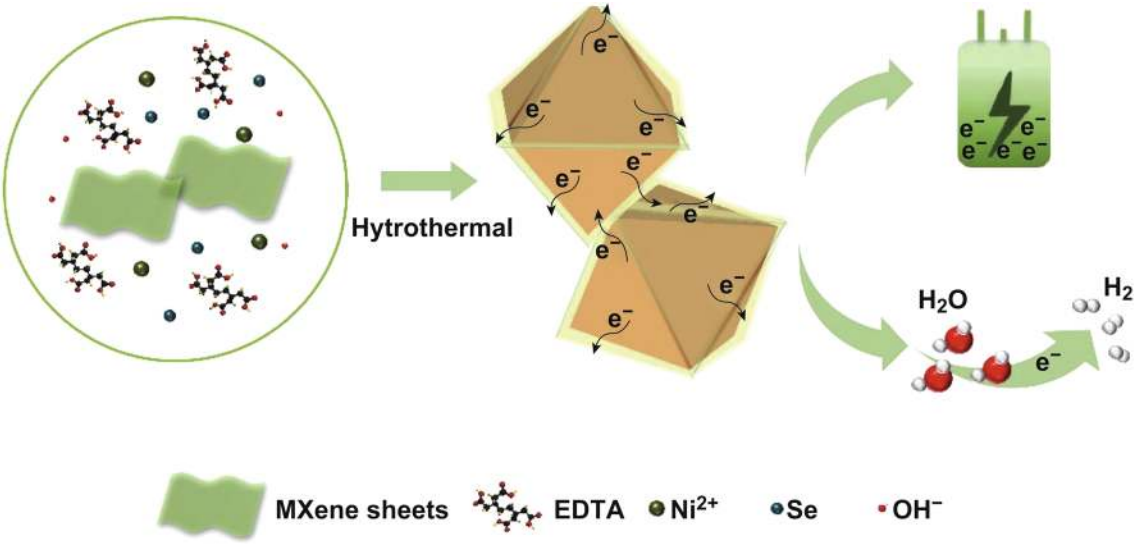

Scheme 1 Schematic illustration for the formation of octahedral $NiSe_2/Ti_3C_2T_x$ hybrid through one-pot hydrothermal method

https://doi.org/10.1007/s40820-019-0261-5

KOH solution, in which Ni(II) coordinated with EDTA first and formed a chelate complex, and thus could make a low concentration of free Ni(II) in the solution, which can prevent the deposition of $NiSeO_3$ before the formation of selenides [51]. And then, the Ni(II) chelate complex could be adsorbed on the surface of $Ti_3C_2T_x$ nanosheet due to the negatively charged terminal groups (–O or –OH). During the hydrothermal process, the electrostatic attraction between $Ti_3C_2T_x$ and Ni(II) chelate complex ensures the $Ti_3C_2T_x$ nanosheets wrapping on the surface of $NiSe_2$ crystal, which results in the close contact between $Ti_3C_2T_x$ and $NiSe_2$, and thus could enhance the electrochemical performance of hybrid for both energy storage and conversion [7].

The morphology of the as-prepared $NiSe_2$ and $NiSe_2/Ti_3C_2T_x$ was characterized by SEM and TEM analyses. As shown in Fig. 1a, b, both unmodified $NiSe_2$ and $NiSe_2/Ti_3C_2T_x$ exhibited a typical octahedral configuration under SEM, with the average sizes around 1 μm. However, the

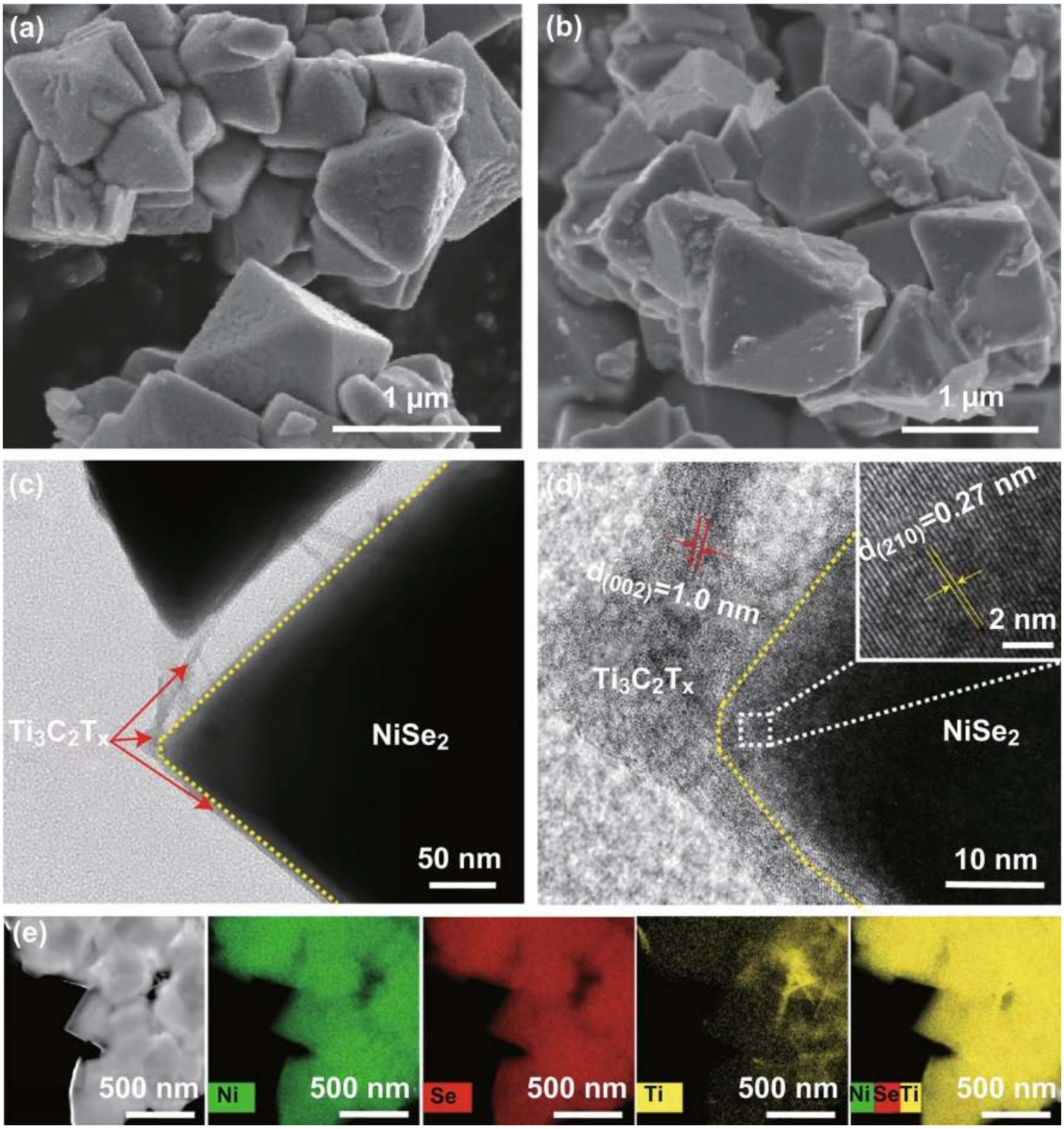

Fig. 1 SEM images of $NiSe_2$ without (**a**) and with $Ti_3C_2T_x$ hybrid (**b**). **c**, **d** TEM image of $NiSe_2/Ti_3C_2T_x$ hybrid in different magnifications. **e** HAADF-STEM image of $NiSe_2/Ti_3C_2T_x$ hybrid and the corresponding EDX elemental mapping of Ni, Se, and Ti elements

surface of the $NiSe_2/Ti_3C_2T_x$ crystal seemed relatively more glazing. Further analysis by TEM revealed that this phenomenon is possibly owing to the ultrathin layer of $Ti_3C_2T_x$ nanosheet evenly covered on the surface of the octahedron-shaped $NiSe_2$ particle (Fig. 1c), which might provide an additional electrical transport path for charge storage or electrocatalysis [53]. Moreover, the high-resolution TEM image in Fig. 1d demonstrates the single crystalline nature of the hybrid. The lattice fringe exhibits an interplanar distance of 0.27 nm, which is in accordance with the spacing of the (210) plane of in $NiSe_2$ single crystal [27]. In addition, the lattice distance of 1.0 nm can be ascribed to the (002) facets of $Ti_3C_2T_x$ nanosheet [38, 41]. It also need to be noted that there is transition phase between $Ti_3C_2T_x$ nanosheet and $NiSe_2$ single crystal, which cannot be well defined. Meanwhile, HAADF-STEM image and the corresponding EDX elemental mapping (Fig. 1e) show that distributions of Ni and Se in $NiSe_2/Ti_3C_2T_x$ hybrid were mostly homogeneous, whereas Ti exhibited the same distribution scale with less density. This also indicates that $Ti_3C_2T_x$ nanosheet should be just evenly wrapped over the surface of $NiSe_2$ crystal. In a word, these results confirmed that the hetero-nanostructure of $NiSe_2/Ti_3C_2T_x$ hybrid is comprised with crystallized $NiSe_2$ octahedral crystal in the ultrathin $Ti_3C_2T_x$ nanosheet cloak. As a conductive layer, the extra $Ti_3C_2T_x$ nanosheet on the surface might be beneficial to strengthen the conductivity as well as the electrochemical activity of the original $NiSe_2$ [7, 34].

The as-prepared $NiSe_2$ and $NiSe_2/Ti_3C_2T_x$ samples were also investigated by XRD. As shown in Fig. 2a, the diffraction peaks of both materials at 29.9° (200), 33.6° (210), 36.9° (211), 42.9° (220), 50.7° (311), 53.2° (222), 55.5° (023), 57.8° (321), 62.2° (400), 72.6° (421), and 74.6° (332) are in well agreement with the pyrite $NiSe_2$ (JCPDS NO. 88-1711), which echoes well with the results from high-resolution TEM, indicating the pyrite crystallized structure for $NiSe_2/Ti_3C_2T_x$ hybrid [20, 26]. Notably, the diffraction peak at 6.7° (002), corresponding to *c* lattice parameter of $Ti_3C_2T_x$ sheet, was not observed in the XRD pattern of $NiSe_2/Ti_3C_2T_x$ hybrid, which is possibly because of the low

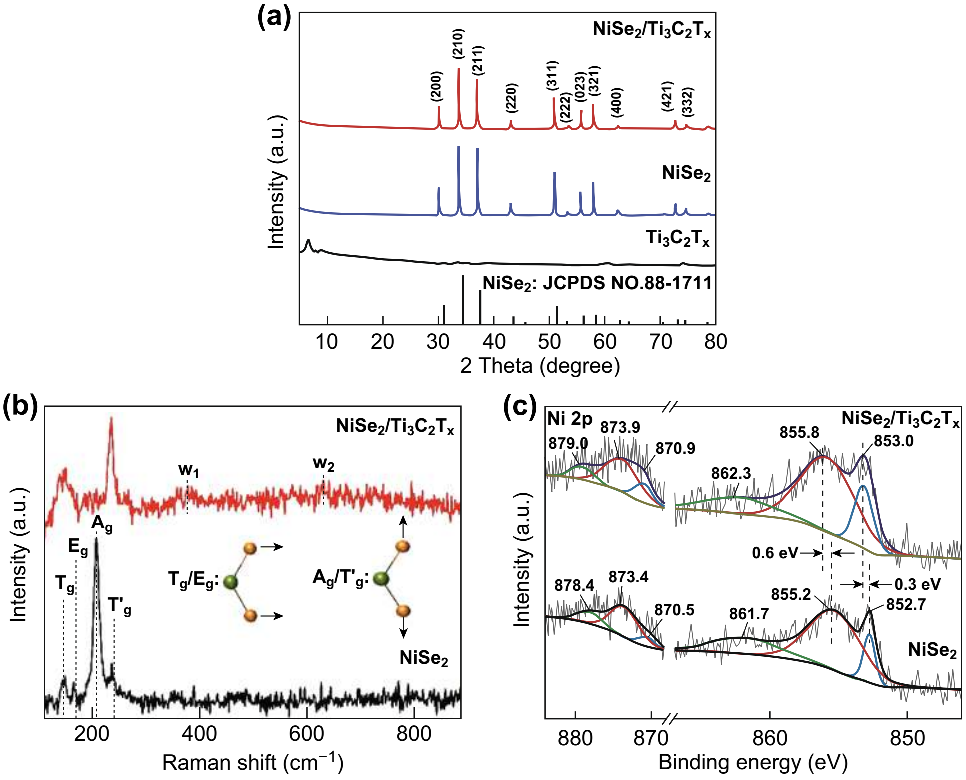

Fig. 2 **a** XRD patterns of unmodified $NiSe_2$ and $NiSe_2/Ti_3C_2T_x$ hybrid. **b** Comparison of Raman spectra for $NiSe_2$ and $NiSe_2/Ti_3C_2T_x$ hybrid, and the inset is atom schematic of $NiSe_2$. (The green ball is Ni atom, and the yellow ball is Se atom.) **c** Ni 2*p* XPS spectra of unmodified $NiSe_2$ and $NiSe_2/Ti_3C_2T_x$ hybrid

content of $Ti_3C_2T_x$ sheet in the hybrid [54]. Despite that, no obvious impurities were detected, indicating high purity and crystallinity for both crystals.

To further understand the interaction between $Ti_3C_2T_x$ nanosheet and $NiSe_2$ crystal in the composite, the Raman spectroscopy was employed. As displayed in Fig. 2b, for $NiSe_2/Ti_3C_2T_x$ hybrid, the four strong peaks (Tg, Eg, Ag, and Tg) at 149, 169, 210, and 240 cm^{-1} are in accordance with the Raman bands of pyrite $NiSe_2$, which assigned to stretching and rotational modes of the Se–Se pairs in $NiSe_2$ molecular, while the two weak peaks (w_1 and w_2) at 380 and 650 cm^{-1} are correlated with the Ti–C vibrations of $Ti_3C_2T_x$ [30, 38]. Compared with the unmodified $NiSe_2$, these four peaks of $NiSe_2/Ti_3C_2T_x$ hybrid obviously red-shift from the original coordinates of 154, 193, 237, and 269 cm^{-1}, which is probably owing to the changing in the surface strain after the coating of $Ti_3C_2T_x$ nanosheet, and also is indicative of a possible strong interfacial interaction between the $NiSe_2$ and $Ti_3C_2T_x$ in hybrid [7].

XPS was carried out to verify the interfacial interaction between $NiSe_2$ and $Ti_3C_2T_x$ (see Fig. S3 for the survey spectra). The Ni 2*p* spectrum has been fitted by considering two resolved doublets with a spin–orbit splitting around 18.0 eV between $2p_{3/2}$ and $2p_{1/2}$ and a fixed area ratio equal to 2:1 (Table S1). As shown in Fig. 2c, the Ni 2*p* spectrum of $NiSe_2/Ti_3C_2T_x$ hybrid exhibits peaks at binding energy of 853.0 and 870.9 eV, corresponding to the Ni $2p_{3/2}$ and Ni $2p_{1/2}$, respectively. The peaks at 855.8 and 873.9 eV are related to the oxidation state of Ni on the surface. Two satellite peaks at 862.3 and 879.0 eV were also observed [27, 55]. Compared with unmodified $NiSe_2$, the characteristic peaks of Ni species from $NiSe_2/Ti_3C_2T_x$ hybrid are obviously shifted by 0.3 and 0.6 eV to higher binding energy. This obvious Ni 2*p* peak-shift toward higher binding energy confirms the strong interactions between $NiSe_2$ and $Ti_3C_2T_x$, which makes the Ni center in $NiSe_2$ more positively charged and thus facilitates the electrostatic attraction of more anionic intermediates for fast redox process [56, 57]. This finding is in decent agreement with the Raman results and may be due to the $Ti_3C_2T_x$ containing rich hydroxyl terminations with high electronegativity, which can strongly interact with $NiSe_2$ [58]. Compared with traditional physical binding (Fig. S4), such binding method might be more efficient for redox process and charge transfer in $NiSe_2/Ti_3C_2T_x$ hybrid, consequently accelerating its electrochemical activities [7, 45].

3.2 Supercapacitor Performance of $NiSe_2$ and $Ti_3C_2T_x$/$NiSe_2$

To evaluate the electrochemical performance of $NiSe_2$/$Ti_3C_2T_x$ hybrid, the $NiSe_2/Ti_3C_2T_x$ hybrid materials and the unmodified $NiSe_2$ were both applied as active materials for supercapacitor, and the electrochemical performance of nickel form substrate was also investigated. From the cyclic voltammetry (CV) curves, the bare nickel form substrate shows very small areas, indicating the low electrochemical activity. As demonstrated in Fig. 3a, the CV curves for unmodified $NiSe_2$ and $NiSe_2/Ti_3C_2T_x$ hybrid exhibit a clear redox pair, which is attributed to the Faradic redox reaction and consistent well with previous reports, suggesting the pseudocapacitive characteristic of $NiSe_2$ [25]. According to the literature, all divalent cations in $NiSe_2$ were transformed into trivalent cations after positive sweep, and the reaction mechanism of charge storage may occur as shown in Eqs. 2 and 3 [24]:

$$NiSe_2 + H_2O + 1/2O_2 \rightarrow Ni(OH)_2 + 2Se \quad (2)$$

$$Ni(OH)_2 + OH^- \leftrightarrow NiOOH + e^- \quad (3)$$

Meanwhile, the paired redox peaks (see Fig. S5 for details) still existed with the increasing scan rate which indicates good ability of rapid oxidation reduction reaction for $NiSe_2$ [15]. However, with the increase in the scan rate, an asymmetry of redox peaks was detected, which may be due to the polarization effect as well as ohmic resistance during the Faradic process [59, 60]. In addition, the symmetrical time of charge and discharge in all cases (see Fig. S6 for details) indicates high coulombic efficiencies of as-prepared electrodes and in good agreement with the CV curves. In particular, $NiSe_2/Ti_3C_2T_x$ hybrid exhibits much larger CV area and longer charge–discharge time (Fig. 3b) compared with the unmodified $NiSe_2$, verifying the higher supercapacitor performance. From the Galvanostatic charging/discharging curves (GCD) curves, the highest specific capacitance of $NiSe_2/Ti_3C_2T_x$ was estimated to be 531.2 F g^{-1} at 1 A g^{-1}, which is 31% larger than that of the unmodified $NiSe_2$ at same current densities. Moreover, a specific capacitance of 348 F g^{-1} for $NiSe_2/Ti_3C_2T_x$ hybrid could still be achieved at a higher current density of 10 A g^{-1}, exhibiting a relatively good rate capability with the retained capacitance of 66%, which is 8% larger than that of the unmodified $NiSe_2$. This considerably enhanced electrochemical performance and improved rate capability of the $NiSe_2/Ti_3C_2T_x$ hybrid which might be caused by the interfacial effect from the interfacial interaction of $Ti_3C_2T_x$, which improves the electrochemical activities of the materials.

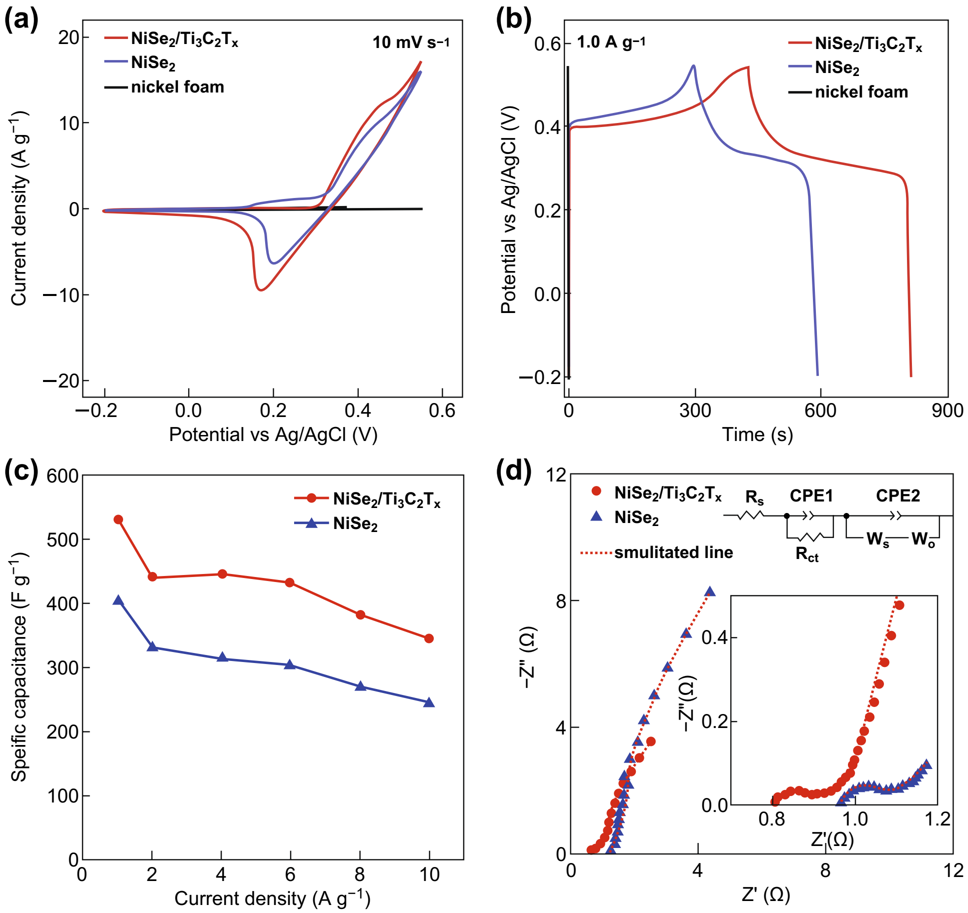

Fig. 3 Supercapacitor performance in 2 M KOH solution: **a** CV profiles of unmodified $NiSe_2$, $NiSe_2/Ti_3C_2T_x$, and bare nickel foam at 10 mV s^{-1}. **b** GCD curves of unmodified $NiSe_2$, $NiSe_2/Ti_3C_2T_x$, and bare nickel foam at 1.0 A g^{-1}. **c** Variation of specific capacitances with current density for unmodified $NiSe_2$ and $NiSe_2/Ti_3C_2T_x$. **d** Nyquist plots of unmodified $NiSe_2$ and $NiSe_2/Ti_3C_2T_x$ in the range of 10 mHz to 100 kHz (inset is the high-frequency region and the equivalent circuit used to fit the experimental data)

To further investigate the inner electrochemical mechanism of the performance facilitating process, the EIS was carried out for both $NiSe_2/Ti_3C_2T_x$ hybrid and unmodified $NiSe_2$. As shown in Fig. 3d, the Nyquist plots for both materials exhibit the similar pattern with two semicircles in the high-frequency region and a linear line in the low frequency area. The first and second semicircles are related to the charge-transfer process and electrolyte infiltration process on the surface, respectively, whereas the linear part is related to finite Nernst diffusion in the surface and semi-infinite Warburg diffusion process in the bulk [12]. In Fig. 3d, a simulated equivalent circuit is introduced to fit the Nyquist plots, where the R_s means solution resistance; CPE1 and CPE2 are constant phase element; R_{ct} represents the charge-transfer resistance; W_s and W_o are the finite Nernst diffusion impedance and semi-infinite Warburg diffusion impedance, respectively [12]. The detailed fitting parameters are included in Table S2. The results manifest a charge-transfer resistance of 95.4 mΩ for $NiSe_2/Ti_3C_2T_x$ hybrid, which is obviously lower than that of unmodified $NiSe_2$ (127.4 mΩ). This reduced charge-transfer resistance for $NiSe_2/Ti_3C_2T_x$ hybrid should be attributed to the enhanced conductivity from the chemical combination of high conductive $Ti_3C_2T_x$ sheet. Meanwhile, the Warburg diffusion resistance of the $NiSe_2/Ti_3C_2T_x$ hybrid is 31.6% smaller than that of unmodified $NiSe_2$, indicating a higher ion diffusion rate. The low diffusion resistance of ion transport should be owing to the two-dimensional morphology and the extra redox active sites from terminal group on the $Ti_3C_2T_x$ sheet surface [40, 44]. In sum, the EIS spectrum analysis demonstrates that the introduction of $Ti_3C_2T_x$ provides lowered charge-transfer resistance as well as enhanced ion diffusion rate, therefore facilitating a higher specific capacitance for $NiSe_2/Ti_3C_2T_x$ hybrid [7].

In addition, the long-term stability of the two samples also has been tested via the GCD method at 4 A g^{-1} (Fig. S7). It showed that the capacitance retention of $NiSe_2/Ti_3C_2T_x$ hybrid is 47.3% larger than that of unmodified $NiSe_2$ after 1000 cycles, suggesting that the $Ti_3C_2T_x$ sheet can also improve the stability of $NiSe_2$ during electrochemical process. This stabilization effect might be attributed to two aspects. Firstly, since the $NiSe_2$ is known to form irreversible oxide counterparts in the electrochemical cycling, the $Ti_3C_2T_x$ sheet can serve as a protective layer from its oxidation [20, 31]. Secondly, similar to the modification on rGO and other 2D carbonaceous materials [61, 62], the interfacial interaction of $Ti_3C_2T_x$ sheet should favor the defective sites on $NiSe_2$ particle surface, which, to a large extent, amends the deficiency of the original $NiSe_2$ nanocrystal. However, these deductions still need further verification in the future.

3.3 HER Performance of $NiSe_2$ and $NiSe_2/Ti_3C_2T_x$

To estimate its potential multifunction, $NiSe_2/Ti_3C_2T_x$ hybrid was employed as the catalytic materials in hydrogen evolution reaction, where the catalytic materials would decrease the reaction barrier. For comparison, HER activity measurements were also performed for the pure $Ti_3C_2T_x$, unmodified $NiSe_2$, 20%Pt/C, and glassy carbon under the same conditions. From LSV curves in Fig. 4a, as expected, the 20% Pt/C displays remarkable HER activity (10 mA cm^{-2} at 44 mV

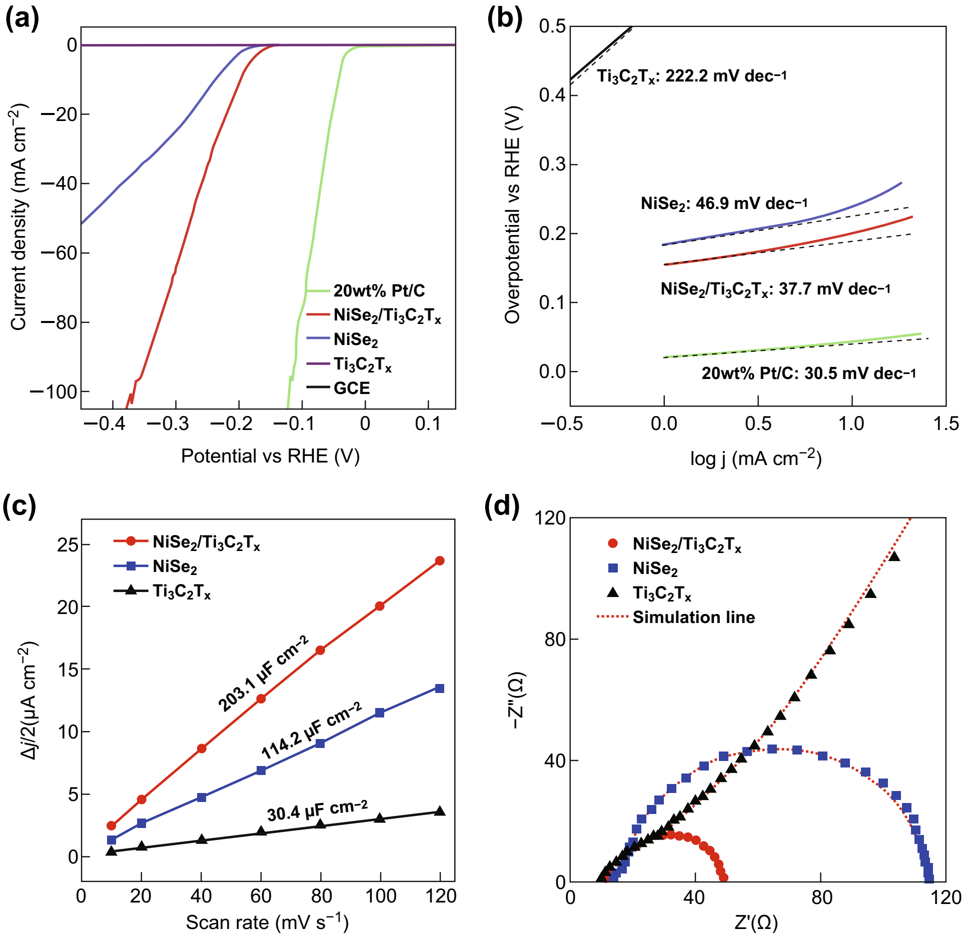

Fig. 4 HER catalytic performance in 0.5 M H_2SO_4 solution: **a** LSV curves of unmodified $NiSe_2$, $NiSe_2/Ti_3C_2T_x$ hybrid, pure $Ti_3C_2T_x$, 20 wt%Pt/C, and glassy carbon electrode at the scan rate of 5 mV s^{-1}. **b** Tafel plots of unmodified $NiSe_2$, $NiSe_2/Ti_3C_2T_x$ hybrid, pure $Ti_3C_2T_x$, and 20 wt%Pt/C. **c** The extracted double-layer capacitances of different electrodes using a cyclic voltammetry method. **d** EIS Nyquist plots in the range of 10 mHz to 100 kHz

vs. RHE), while pure $Ti_3C_2T_x$ and glassy carbon display no obvious catalytic activity for H_2 evolution. In contrasted, the $NiSe_2/Ti_3C_2T_x$ exhibits an enormous increase in the cathodic current density compared with the $NiSe_2$ and the $Ti_3C_2T_x$, exhibiting an overpotential of 200.0 mV at a current density of 10 mA cm^{-2}, which is lower than unmodified $NiSe_2$ of 239.0 mV under the same current density. Moreover, the overpotential required for the $NiSe_2/Ti_3C_2T_x$ hybrid and unmodified $NiSe_2$ to produce a current density of 45 mA cm^{-2} is 269.0 and 418.1 mV, respectively. It is obvious that the $NiSe_2/Ti_3C_2T_x$ hybrid possesses a better HER catalytic activity than unmodified $NiSe_2$. The enhanced performance of the $NiSe_2/Ti_3C_2T_x$ electrode can be attributed to the charge transfer from $NiSe_2$ to $Ti_3C_2T_x$, which may provide a faster adsorption kinetics and higher utilization of active sites for high HER efficiency [14].

In order to demonstrate the kinetics of the electrodes during the HER process, the Tafel analysis was carried out on the polarization curve. As shown in Fig. 4b, the $NiSe_2/Ti_3C_2T_x$ hybrid with low Tafel slope of 37.7 mV dec^{-1} is nearly comparable to that of Pt catalyst (30.5 mV dec^{-1}) and smaller than that of the unmodified $NiSe_2$ (46.9 mV dec^{-1}) as well as unmodified $Ti_3C_2T_x$ (222.2 mV dec^{-1}), which implies that the electrocatalytic reaction follows the Volmer–Heyrovsky pathway for the $NiSe_2/Ti_3C_2T_x$ hybrid [7]. In addition, the exchange current density (j_0) at the thermodynamic redox potential ($\eta = 0$), another key factor to evaluate catalytic property, can be extracted by extrapolating the Tafel plots to the x-axis [30]. The j_0 value (147.5 μA cm^{-2}) for the $NiSe_2/Ti_3C_2T_x$ hybrid is higher than that of the unmodified $NiSe_2$ (56.8 μA cm^{-2}), indicating a better catalytic activity of the $NiSe_2/Ti_3C_2T_x$ hybrid (Table S3). These results clearly demonstrate an enhanced catalytic performance of $NiSe_2/Ti_3C_2T_x$ hybrid, which is possibly owing to the interfacial interaction between the $Ti_3C_2T_x$ sheet and $NiSe_2$ crystal, inducing the charge-transfer process. As shown in Figs. 4c and S8, the double-layer capacitance C_{dl} for $NiSe_2/Ti_3C_2T_x$ hybrid (203.1 μF cm^{-2}) also exhibits large improvement compared with unmodified $NiSe_2$ (114.2 μF cm^{-2}), which suggests that the $Ti_3C_2T_x$ sheet wrapping on $NiSe_2$ surface not only facilitates changer transfer, but also improves the utilization of active site as well [32].

The EIS measurements in 0.5 M H_2SO_4 electrolyte provide further details on the enhanced HER process. As shown in Fig. 4d, the Nyquist plots are fitted by equivalent circuit model (Fig. S9) [63], and the simulated parameters are summarized in Table S2. The $NiSe_2/Ti_3C_2T_x$ hybrid exhibits the lower R_{ct} (33.9 Ω) than that of unmodified $NiSe_2$ (95.7 Ω), indicating a higher electrochemical reaction rate and more efficient charge-transfer process for hybrid [64]. This enhanced conductivity could result from the chemical coupling with $Ti_3C_2T_x$ sheet, a better conductor. Consequently, the high conductivity of the $NiSe_2/Ti_3C_2T_x$ hybrid guarantees the higher apparent catalytic activity toward HER since less potential is needed for driving the current transport across the catalyst [48]. In addition, the long-term stability test revealed a superior durability of the $NiSe_2/Ti_3C_2T_x$ hybrid (Fig. S10), where the $NiSe_2/Ti_3C_2T_x$ hybrid showed negligible degradation in the current density after 2000 cycles, which is also positively related to the combination of $Ti_3C_2T_x$ sheet [33]. To demonstrate further the good stability, time-dependent current density curve for $NiSe_2/Ti_3C_2T_x$ under constant overpotential of -0.25 V versus RHE was also conducted for 10 h. As shown in Fig. S11, the current density of the $NiSe_2/Ti_3C_2T_x$ hybrid has slight decrease compared with pure $NiSe_2$.

In general, certain requirements such as good electrical conductivity, robust structure, large active surface area, and fast diffusion pathway, are applicable to achieve high-performance materials for energy storage and electrocatalysis [48]. The unique structural superiorities make $NiSe_2/Ti_3C_2T_x$ hybrid a well-fit candidate for these demands. Firstly, the $NiSe_2$ are stabilized by $Ti_3C_2T_x$ MXene sheet wrapping on the surface, and their outstanding electrical properties are secured. Moreover, the $Ti_3C_2T_x$ MXene sheet significantly promotes the electronic coupling by acting as the 2D conductive linker for fast charge transfer. Finally, the functional terminal group on $Ti_3C_2T_x$ MXene surface provides the possibility for chemical coupling with $NiSe_2$ crystal, which enables the strong interfacial interaction for fast charge transfer and high stability against repeated electrochemical cycling as well. These advantages for the synergism of $NiSe_2$ crystal and $Ti_3C_2T_x$ MXene sheet have led to a remarkable improvement in electrochemical activity and durability for supercapacitor and HER. Furthermore, compared with recently reported supercapacitor materials and HER catalysts (Table S4 and Table S5, respectively), the $NiSe_2/Ti_3C_2T_x$ hybrid has shown superior performance, verifying an enormous potential in multifunctional applications.

https://doi.org/10.1007/s40820-019-0261-5

4 Conclusions

In summary, a novel $NiSe_2/Ti_3C_2T_x$ hybrid has been successfully synthesized, by wrapping $NiSe_2$ octahedral crystal with ultrathin $Ti_3C_2T_x$ MXene nanosheet via a one-pot hydrothermal method. Its composition and morphology have been analyzed through varies techniques, establishing a strong interfacial interaction between $NiSe_2$ octahedral crystal and the evenly distributed ultrathin $Ti_3C_2T_x$ MXene nanosheet layer on its surface. A high specific capacitance of 531.2 F g^{-1} at 1 A g^{-1} for supercapacitor, low overpotential of 200 mV at 10 mA g^{-1}, and small Tafel slope of 37.7 mV dec^{-1} for HER are achieved by employing $NiSe_2/Ti_3C_2T_x$ hybrid as the electrode material. Furthermore, greater cycling stabilities for $NiSe_2/Ti_3C_2T_x$ hybrid in both supercapacitor and HER have also been achieved. These significant improvements compared with unmodified $NiSe_2$ should be owing to the strong interfacial interaction between $NiSe_2$ octahedral crystal and $Ti_3C_2T_x$ MXene which provides enhanced conductivity, faster charge transfer as well as more abundant active sites and also highlight the promising potentials in combinations of MXene with metal selenides for multifunctional applications such as energy storage and conversion.

Acknowledgements This research was supported by Grants from the Danish National Research Foundation, AUFF-NOVA project from Aarhus Universitets Forsknings fund, EU H2020RISE 2016-MNR4SCell project, National Natural Science Foundation of China (Nos. 21528501, 51272296, and 51571195), and the Chongqing Graduate Student Research Innovation Project (No. CYB15046). We also gratefully acknowledge support from the Key Program of the Chinese Academy of Sciences (KJZD-EW-M05-3). H. Jiang greatly appreciates the financial support of China Scholarship Council (CSC). Z. Wang thanks the support of Fundamental Research Funds for the Central Universities, China (YJ201893).

Electronic supplementary material The online version of this article (https://doi.org/10.1007/s40820-019-0261-5) contains supplementary material, which is available to authorized users.

References

1. Z.P. Cano, D. Banham, S.Y. Ye, A. Hintennach, J. Lu, M. Fowler, Z.W. Chen, Batteries and fuel cells for emerging electric vehicle markets. Nat. Energy **3**(4), 279–289 (2018). https://doi.org/10.1038/s41560-018-0108-1
2. W. Zeng, L. Shu, Q. Li, S. Chen, F. Wang, X.M. Tao, Fiber-based wearable electronics: a review of materials, fabrication, devices, and applications. Adv. Mater. **26**(31), 5310–5336 (2014). https://doi.org/10.1002/adma.201400633
3. L. Li, Z. Wu, S. Yuan, X.B. Zhang, Advances and challenges for flexible energy storage and conversion devices and systems. Energy Environ. Sci. **7**(7), 2101–2122 (2014). https://doi.org/10.1039/c4ee00318g
4. Y. Yang, H.L. Fei, G.D. Ruan, C.S. Xiang, J.M. Tour, Edge-oriented MoS_2 nanoporous films as flexible electrodes for hydrogen evolution reactions and supercapacitor devices. Adv. Mater. **26**(48), 8163–8168 (2014). https://doi.org/10.1002/adma.201402847
5. X. Liu, J. Iocozzia, Y. Wang, X. Cui, Y. Chen, S. Zhao, Z. Li, Z. Lin, Noble metal–metal oxide nanohybrids with tailored nanostructures for efficient solar energy conversion, photocatalysis and environmental remediation. Energy Environ. Sci. **10**(2), 402–434 (2017). https://doi.org/10.1039/c6ee02265k
6. J.M. Wei, M. Zhou, A.C. Long, Y.M. Xue, H.B. Liao, C. Wei, Z.C.J. Xu, Heterostructured electrocatalysts for hydrogen evolution reaction under alkaline conditions. Nano-Micro Lett. **10**(4), 75–84 (2018). https://doi.org/10.1007/s40820-018-0229-x
7. J. Yang, C. Wang, H. Ju, Y. Sun, S. Xing, J. Zhu, Q. Yang, Integrated quasiplane heteronanostructures of $MoSe_2/Bi_2Se_3$ hexagonal nanosheets: synergetic electrocatalytic water splitting and enhanced supercapacitor performance. Adv. Funct. Mater. **27**(48), 1703864 (2017). https://doi.org/10.1002/adfm.201703864
8. S. Li, C. Cheng, X. Zhao, J. Schmidt, A. Thomas, Active salt/silica-templated 2D mesoporous FeCo-N_x-carbon as bifunctional oxygen electrodes for zinc–air batteries. Angew. Chem. Int. Ed. **57**(7), 1856–1862 (2018). https://doi.org/10.1002/anie.201710852
9. S. Li, C. Cheng, A. Sagaltchik, P. Pachfule, C.S. Zhao, A. Thomas, Metal–organic precursor-derived mesoporous carbon spheres with homogeneously distributed molybdenum carbide/nitride nanoparticles for efficient hydrogen evolution in alkaline media. Adv. Funct. Mater. **29**(3), 1807419 (2019). https://doi.org/10.1002/adfm.201807419
10. X. Tian, X. Li, T. Yang, Y. Song, Z. Liu, Q. Guo, Recent advances on synthesis and supercapacitor application of binary metal oxide. J. Inorg. Mater. **32**(5), 459–468 (2017). https://doi.org/10.15541/jim20160452
11. G.C. Lau, N.A. Sather, H. Sai, E.M. Waring, E. Deiss-Yehiely et al., Oriented multiwalled organic–$Co(OH)_2$ nanotubes for energy storage. Adv. Funct. Mater. **28**(3), 1702320 (2018). https://doi.org/10.1002/adfm.201702320
12. Z. Fan, J. Liang, W. Yu, S. Ding, S. Cheng et al., Ultrathin NiO nanosheets anchored on a highly ordered nanostructured

carbon as an enhanced anode material for lithium ion batteries. Nano Energy **16**, 152–162 (2015). https://doi.org/10.1016/j.nanoen.2015.06.009

13. X. Yang, K. Xu, R. Zou, J. Hu, A hybrid electrode of Co_3O_4@PPy core/shell nanosheet arrays for high-performance supercapacitors. Nano-Micro Lett. **8**(2), 143–150 (2016). https://doi.org/10.1007/s40820-015-0069-x
14. J. Wang, F. Xu, H.Y. Jin, Y.Q. Chen, Y. Wang, Non-noble metal-based carbon composites in hydrogen evolution reaction: fundamentals to applications. Adv. Mater. **29**(14), 1605838 (2017). https://doi.org/10.1002/Adma.201605838
15. T. Chen, S. Li, J. Wen, P. Gui, G. Fang, Metal–organic framework template derived porous $CoSe_2$ nanosheet arrays for energy conversion and storage. ACS Appl. Mater. Interfaces **9**(41), 35927–35935 (2017). https://doi.org/10.1021/acsami.7b12403
16. Z. Wang, Q. Li, Y. Chen, B. Cui, Y. Li, F. Besenbacher, M. Dong, The ambipolar transistor behavior of WSe_2 transistors and its analogue circuits. NPG Asia Mater. **10**, 703–712 (2018). https://doi.org/10.1038/s41427-018-0062-1
17. Z.G. Wang, Q. Li, F. Besenbacher, M.D. Dong, Facile synthesis of single crystal $PtSe_2$ nanosheets for nanoscale electronics. Adv. Mater. **28**(46), 10224–10229 (2016). https://doi.org/10.1002/adma.201602889
18. L. Xie, Z. Yang, J. Sun, H. Zhou, X. Cui et al., Bi_2Se_3/C nanocomposite as a new sodium-ion battery anode material. Nano Micro Lett. **10**(3), 50 (2018). https://doi.org/10.1007/s40820-018-0201-9
19. H. Fan, H. Yu, X. Wu, Y. Zhang, Z. Luo et al., Controllable preparation of square nickel chalcogenide (NiS and $NiSe_2$) nanoplates for superior Li/Na ion storage properties. ACS Appl. Mater. Interfaces **8**(38), 25261–25267 (2016). https://doi.org/10.1021/acsami.6b07300
20. X. Ou, J. Li, F. Zheng, P. Wu, Q. Pan, X. Xiong, C. Yang, M. Liu, In situ X-ray diffraction characterization of $NiSe_2$ as a promising anode material for sodium ion batteries. J. Power Sources **343**, 483–491 (2017). https://doi.org/10.1016/j.jpowsour.2017.01.097
21. S. Zhu, Q. Li, Q. Wei, R. Sun, X. Liu, Q. An, L. Mai, $NiSe_2$ nanooctahedra as an anode material for high-rate and long-life sodium-ion battery. ACS Appl. Mater. Interfaces **9**(1), 311–316 (2017). https://doi.org/10.1021/acsami.6b10143
22. M. Lu, X.P. Yuan, X.H. Guan, G.S. Wang, Synthesis of nickel chalcogenide hollow spheres using an L-cysteine-assisted hydrothermal process for efficient supercapacitor electrodes. J. Mater. Chem. A **5**(7), 3621–3627 (2017). https://doi.org/10.1039/c6ta10426f
23. K. Guo, F. Yang, S. Cui, W. Chen, L. Mi, Controlled synthesis of 3D hierarchical NiSe microspheres for high-performance supercapacitor design. RSC Adv. **6**(52), 46523–46530 (2016). https://doi.org/10.1039/c6ra06909f
24. W. Wei, L. Mi, Y. Gao, Z. Zheng, W. Chen, X. Guan, Partial ion-exchange of nickel-sulfide-derived electrodes for high performance supercapacitors. Chem. Mater. **26**(11), 3418–3426 (2014). https://doi.org/10.1021/cm5006482
25. A. Chang, C. Zhang, Y. Yu, Y. Yu, B. Zhang, Plasma-assisted synthesis of $NiSe_2$ ultrathin porous nanosheets with selenium vacancies for supercapacitor. ACS Appl. Mater. Interfaces **10**, 4161–4165 (2018). https://doi.org/10.1021/acsami.8b16072
26. B. Yu, X. Wang, F. Qi, B. Zheng, J. He et al., Self-assembled coral-like hierarchical architecture constructed by $NiSe_2$ nanocrystals with comparable hydrogen-evolution performance of precious platinum catalyst. ACS Appl. Mater. Interfaces **9**(8), 7154–7159 (2017). https://doi.org/10.1021/acsami.6b15719
27. J. Liang, Y. Yang, J. Zhang, J. Wu, P. Dong, J. Yuan, G. Zhang, J. Lou, Metal diselenide nanoparticles as highly active and stable electrocatalysts for the hydrogen evolution reaction. Nanoscale **7**(36), 14813–14816 (2015). https://doi.org/10.1039/c5nr03724g
28. Z. Gao, J. Qi, M. Chen, W. Zhang, R. Cao, An electrodeposited NiSe for electrocatalytic hydrogen and oxygen evolution reactions in alkaline solution. Electrochim. Acta **224**, 412–418 (2017). https://doi.org/10.1016/j.electacta.2016.12.070
29. Q.L. Liu, Y.J. Dong, Y. Cao, H.Y. Chen, D.B. Kuang, C.Y. Su, Ni_xS_y/$NiSe_2$ hybrid catalyst grown in situ on conductive glass substrate as efficient counter electrode for dye-sensitized solar cells. Electrochim. Acta **250**, 244–250 (2017). https://doi.org/10.1016/j.electacta.2017.08.085
30. Z. Wang, H.H. Wu, Q. Li, F. Besenbacher, X.C. Zeng, M. Dong, Self-scrolling MoS_2 metallic wires. Nanoscale **10**, 18178–18185 (2018). https://doi.org/10.1039/c8nr04611e
31. P. Zhang, Z. Wang, L. Liu, L.H. Klausen, Y. Wang, J.L. Mi, M. Dong, Modulation the electronic property of 2D monolayer MoS_2 by amino acid. Appl. Mater. Today **14**, 151–158 (2019). https://doi.org/10.1016/j.apmt.2018.12.003
32. D.Y. Song, H.Q. Wang, X.Q. Wang, B. Yu, Y.F. Chen, $NiSe_2$ nanoparticles embedded in carbon nanowires as highly efficient and stable electrocatalyst for hydrogen evolution reaction. Electrochim. Acta **254**, 230–237 (2017). https://doi.org/10.1016/j.electacta.2017.09.056
33. S. Zheng, L. Zheng, Z. Zhu, J. Chen, J. Kang, Z. Huang, D. Yang, MoS_2 nanosheet arrays rooted on hollow rGO spheres as bifunctional hydrogen evolution catalyst and supercapacitor electrode. Nano-Micro Lett. **10**(4), 62–72 (2018). https://doi.org/10.1007/s40820-018-0215-3
34. Q.H. Wang, C. Guo, Y.X. Zhu, J.P. He, H.Q. Wang, Reduced graphene oxide-wrapped FeS_2 composite as anode for high-performance sodium-ion batteries. Nano-Micro Lett. **10**(2), 30–40 (2018). https://doi.org/10.1007/s40820-017-0183-z
35. Y.Y. Peng, B. Akuzum, N. Kurra, M.Q. Zhao, M. Alhabe et al., All-MXene (2D titanium carbide) solid-state microsupercapacitors for on-chip energy storage. Energy Environ. Sci. **9**(9), 2847–2854 (2016). https://doi.org/10.1039/c6ee01717g
36. M. Beidaghi, Y. Gogotsi, Capacitive energy storage in microscale devices: recent advances in design and fabrication of micro-supercapacitors. Energy Environ. Sci. **7**(3), 867–884 (2014). https://doi.org/10.1039/c3ee43526a
37. M.R. Lukatskaya, O. Mashtalir, C.E. Ren, Y. Dall'Agnese, P. Rozier et al., Cation intercalation and high volumetric

capacitance of two-dimensional titanium carbide. Science **341**(6153), 1502–1505 (2013). https://doi.org/10.1126/science.1241488

38. M. Naguib, M. Kurtoglu, V. Presser, J. Lu, J. Niu et al., Two-dimensional nanocrystals produced by exfoliation of Ti_3AlC_2. Adv. Mater. **23**(37), 4248–4253 (2011). https://doi.org/10.1002/adma.201102306
39. M. Naguib, V.N. Mochalin, M.W. Barsoum, Y. Gogotsi, 25th Anniversary article: MXenes: a new family of two-dimensional materials. Adv. Mater. **26**(7), 992–1005 (2014). https://doi.org/10.1002/adma.201304138
40. M.R. Lukatskaya, S. Kota, Z. Lin, M.Q. Zhao, N. Shpigel et al., Ultra-high-rate pseudocapacitive energy storage in two-dimensional transition metal carbides. Nat. Energy **2**(8), 17105 (2017). https://doi.org/10.1038/nenergy.2017.105
41. M. Ghidiu, M.R. Lukatskaya, M.Q. Zhao, Y. Gogotsi, M.W. Barsoum, Conductive two-dimensional titanium carbide 'clay' with high volumetric capacitance. Nature **516**(7529), 78–81 (2014). https://doi.org/10.1038/nature13970
42. C.J. Zhang, B. Anasori, A. Seral-Ascaso, S.H. Park, N. McEvoy et al., Transparent, flexible, and conductive 2D titanium carbide (MXene) films with high volumetric capacitance. Adv. Mater. **29**(36), 1702678 (2017). https://doi.org/10.1002/adma.201702678
43. M.Q. Zhao, M. Torelli, C.E. Ren, M. Ghidiu, Z. Ling, B. Anasori, M.W. Barsoum, Y. Gogotsi, 2D titanium carbide and transition metal oxides hybrid electrodes for Li-ion storage. Nano Energy **30**, 603–613 (2016). https://doi.org/10.1016/j.nanoen.2016.10.062
44. M. Hu, T. Hu, Z. Li, Y. Yang, R. Cheng, J. Yang, C. Cui, X. Wang, Surface functional groups and interlayer water determine the electrochemical capacitance of $Ti_3C_2T_x$ MXene. ACS Nano **12**(4), 3578–3586 (2018). https://doi.org/10.1021/acsnano.8b00676
45. H.M. Jiang, Z.G. Wang, Q. Yang, M. Hanif, Z.M. Wang, L.C. Dong, M.D. Dong, A novel $MnO_2/Ti_3C_2T_x$ MXene nanocomposite as high performance electrode materials for flexible supercapacitors. Electrochim. Acta **290**, 695–703 (2018). https://doi.org/10.1016/j.electacta.2018.08.096
46. J.L.C. Tian, Y. Ma, M. Jaroniec, S.Z. Qiao, Interacting carbon nitride and titanium carbide nanosheets for high performance oxygen evolution. Angew. Chem. Int. Ed. **55**, 1138–1142 (2016). https://doi.org/10.1002/anie.201509758
47. L. Zhao, B. Dong, S. Li, L. Zhou, L. Lai et al., Interdiffusion reaction-assisted hybridization of two-dimensional metal-organic frameworks and $Ti_3C_2T_x$ nanosheets for electrocatalytic oxygen evolution. ACS Nano **11**(6), 5800–5807 (2017). https://doi.org/10.1021/acsnano.7b01409
48. X. Wu, Z. Wang, M. Yu, L. Xiu, J. Qiu, Stabilizing the MXenes by carbon nanoplating for developing hierarchical nanohybrids with efficient lithium storage and hydrogen evolution capability. Adv. Mater. **29**(24), 1607017 (2017). https://doi.org/10.1002/adma.201607017
49. N.S. Arul, J.I. Han, Facile hydrothermal synthesis of hexapod-like two dimensional dichalcogenide $NiSe_2$ for supercapacitor. Mater. Lett. **181**, 345–349 (2016). https://doi.org/10.1016/j.matlet.2016.06.065
50. T. Chen, S.Z. Li, J. Wen, P.B. Gui, Y.X. Guo, C. Guan, J.P. Liu, G.J. Fang, Rational construction of hollow core-branch $CoSe_2$ nanoarrays for high-performance asymmetric supercapacitor and efficient oxygen evolution. Small **14**(5), 8 (2018). https://doi.org/10.1002/smll.201700979
51. Z. Zhuang, Q. Peng, J. Zhuang, X. Wang, Y. Li, Controlled hydrothermal synthesis and structural characterization of a nickel selenide series. Chem. Eur. J. **12**(1), 211–217 (2006). https://doi.org/10.1002/chem.200500724
52. T.A. Babkova, H. Fei, N.E. Kazantseva, I.Y. Sapurina, P. Saha, Enhancing the supercapacitor performance of flexible $MnO_{(x)}$Carbon cloth electrodes by Pd-decoration. Electrochim. Acta **272**, 1–10 (2018). https://doi.org/10.1016/j.electacta.2018.03.143
53. G.H. Yu, L.B. Hu, N.A. Liu, H.L. Wang, M. Vosgueritchian, Y. Yang, Y. Cui, Z.A. Bao, Enhancing the supercapacitor performance of graphene/MnO_2 nanostructured electrodes by conductive wrapping. Nano Lett. **11**(10), 4438–4442 (2011). https://doi.org/10.1021/nl2026635
54. Z. Wang, Q. Li, H. Xu, C. Dahl-Petersen, Q. Yang et al., Controllable etching of MoS_2 basal planes for enhanced hydrogen evolution through the formation of active edge sites. Nano Energy **49**, 634–643 (2018). https://doi.org/10.1016/j.nanoen.2018.04.067
55. Y. Zhao, Z. Song, X. Li, Q. Sun, N. Cheng, S. Lawes, X. Sun, Metal organic frameworks for energy storage and conversion. Energy Storage Mater. **2**, 35–62 (2016). https://doi.org/10.1016/j.ensm.2015.11.005
56. M. Yu, S. Zhou, Z. Wang, J. Zhao, J. Qiu, Boosting electrocatalytic oxygen evolution by synergistically coupling layered double hydroxide with MXene. Nano Energy **44**, 181–190 (2018). https://doi.org/10.1016/j.nanoen.2017.12.003
57. H.X. Liu, X.J. Liu, Z.Y. Mao, Z. Zhao, X.Y. Peng, J. Luo, X.M. Sun, Plasma-activated $Co_3(PO_4)(2)$ nanosheet arrays with Co^{3+}-rich surfaces for overall water splitting. J. Power Sources **400**, 190–197 (2018). https://doi.org/10.1016/j.jpowsour.2018.08.028
58. Z.L. Li, Z.C. Zhuang, F. Lv, H. Zhu, L. Zhou et al., The marriage of the FeN_4 moiety and MXene boosts oxygen reduction catalysis: Fe 3D electron delocalization matters. Adv. Mater. **30**(43), 1803220 (2018). https://doi.org/10.1002/Adma.201803220
59. X. Qing, S. Liu, K. Huang, K. Lv, Y. Yang, Z. Lu, D. Fang, X. Liang, Facile synthesis of Co_3O_4 nanoflowers grown on Ni foam with superior electrochemical performance. Electrochim. Acta **56**(14), 4985–4991 (2011). https://doi.org/10.1016/j.electacta.2011.03.118
60. H. Wang, J.J. Zhu, J.M. Zhu, H. Chen, Sonochemical method for the preparation of bismuth sulfide nanorods. J. Phys. Chem. B **106**(15), 3848–3854 (2002). https://doi.org/10.1021/jp0135003
61. Z. Wang, Y. Chen, P. Li, J. He, W. Zhang, Z. Guo, Y. Li, M. Dong, Synthesis of silicon-doped reduced graphene oxide and its applications in dye-sensitive solar cells and

supercapacitors. RSC Adv. **6**(18), 15080–15086 (2016). https://doi.org/10.1039/c5ra25962b

62. S.B. Li, Z.F. Wang, H.M. Jiang, L.M. Zhang, J.Z. Ren et al., Plasma-induced highly efficient synthesis of boron doped reduced graphene oxide for supercapacitors. Chem. Commun. **52**(73), 10988–10991 (2016). https://doi.org/10.1039/c6cc04052g
63. H.A. Bandal, A.R. Jadhav, A.H. Tamboli, H. Kim, Bimetallic iron cobalt oxide self-supported on Ni-Foam: an efficient bifunctional electrocatalyst for oxygen and hydrogen evolution reaction. Electrochim. Acta **249**, 253–262 (2017). https://doi.org/10.1016/j.electacta.2017.07.178
64. Z. Chen, K. Leng, X. Zhao, S. Malkhandi, W. Tang et al., Interface confined hydrogen evolution reaction in zero valent metal nanoparticles-intercalated molybdenum disulfide. Nat. Commun. **8**, 14548 (2017). https://doi.org/10.1038/ncomms14548